Delft University of Technology

Realization and assessment of metal additive manufacturing and topology optimization for high-precision motion systems

Delissen, Arnoud; Boots, Elwin; Laro, Dick; Kleijnen, Harry; van Keulen, Fred; Langelaar, Matthijs

Important note
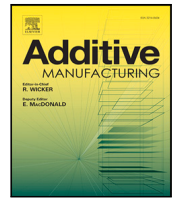To cite this publication, please use the final published version (if applicable).
Please check the document version above.

Research paper

Realization and assessment of metal additive manufacturing and topology optimization for high-precision motion systems

Arnoud Delissen [a],[*], Elwin Boots [b], Dick Laro [b], Harry Kleijnen [c], Fred van Keulen [a], Matthijs Langelaar [a]

[a] *Delft University of Technology, Delft, The Netherlands*
[b] *MI-Partners, Veldhoven, The Netherlands*
[c] *Additive Industries, Eindhoven, The Netherlands*

ARTICLE INFO

ABSTRACT

The design of high-precision motion stages, which must exhibit high dynamic performance, is a challenging task. Manual design is difficult, time-consuming, and leads to sub-optimal designs that fail to fully exploit the extended geometric freedom that additive manufacturing offers. By using topology optimization and incorporating all manufacturing steps (printing, milling, and assembly) into the optimization formulation, high-quality optimized and manufacturable designs can be obtained in an automated manner. With a special focus on overhang control, minimum feature size, and computational effort, the proposed methodology is demonstrated using a case study of an industrial motion stage, optimized for maximum eigenfrequencies. For this case study, an optimized design can be obtained in a single day, showing a substantial performance increase of around 15% as compared to a conventional design. The generated design is manufactured using laser powder-bed fusion in aluminum and experimentally validated within 1% of the simulated performance. This shows that the combination of additive manufacturing and topology optimization can enable significant gains in the high-tech industry.

1. Introduction

The combination of additive manufacturing (AM) and topology optimization has long been promised as a perfect marriage. However, the step from theory to practice has been mostly limited to components intended for use as static structures (see, *e.g.*, [1,2]). In more demanding applications, such as semiconductor equipment, robotics, microscopy, medical devices, and micro-electromechanical devices, extreme dynamic performance is usually required [3,4]. Studies on the combination of AM and topology optimization with realistic complexity for these high-tech applications are scarce, which is surprising, since especially in such applications the potential of this combination is expected to be significant.

The high-tech industry relies on motion systems, *e.g.* for high-precision positioning of samples in microscopy and of wafers and components in the semiconductor industry [3]. Better and better performance is demanded for future targets, and the time-to-market is crucial in this field [4]. Manual design of motion systems is a time-intensive process, where a design is iterated between mechanical designers, dynamics engineers, manufacturing experts, and control specialists. The eigenfrequencies of the system are often limiting the performance (*i.e.*

bandwidth) and a higher bandwidth can generally be obtained by increasing the eigenfrequencies [5].

With metal AM technology maturing, a vastly increased range of geometries can be manufactured as compared to traditional machining processes, enabling potential for enhanced performance. However, it also further complicates the design process for engineers aiming to fully exploit this potential in terms of performance.

The potential of AM can be systematically exploited by using topology optimization, where an optimized design is generated in an automated manner [6]. Much literature is already available on how to incorporate the remaining limitations of AM into the optimization (see, *e.g.*, [7–12]). However, little experimental data and industrial applications can be found beyond simple monolithic brackets based on the maximization of stiffness (see, *e.g.*, [1,2]). For complex applications in the high-tech industry, the usage of topology optimization is not straightforward. The performance of dynamic systems also depends on the mass distribution next to its stiffness. Despite many theoretical examples of dynamical (*i.e.* eigenfrequency) optimizations [13–15], the gap towards practical implementation is still significant, particularly in

---

the context of high-precision motion systems produced with metal additive manufacturing. Here, three main challenges are identified, which apply to many complex design applications in the high-tech domain and beyond. The challenges include various aspects of manufacturability, design resolution (*i.e.* computational cost), and assessment of performance by experimental validation.

Manufacturing. A manufacturing process usually requires a multi-step sequence, which does not only involve AM (laser powder-bed fusion), but also milling to obtain the necessary surface finish and accuracy. Additionally, different components are assembled together to form a system. As each component affects the stiffness and mass distribution, it is critical to evaluate the performance of the entire assembled system. While only the performance of the complete system is evaluated, all preceding manufacturing steps must be represented in the optimization process in order to arrive at a realizable design. First of all, the AM process imposes an overhang angle restriction everywhere in the structure. Secondly, small and fragile features need to be prevented to avoid local overheating and/or warping during manufacturing. Thirdly, the support structures required for the AM process can be removed by milling after printing, but the amount of support structures needs to be minimized as well in order to limit build time and material use. Next to that, sufficient material is required to attach components at interface locations, for instance with bolts. It is essential to incorporate these practical considerations in the optimization, otherwise accounting for them through modifications afterward will inevitably degrade the performance of the obtained design. Additionally, these modifications may be tedious to apply and would needlessly require additional design time.

Design resolution. A higher design resolution in topology optimization corresponds to more freedom in representing geometric features. Additive manufacturing provides a very high spatial resolution, which ideally should correspond to the design resolution of topology optimization. However, having a fine design resolution inflicts a large computational burden, especially since eigenfrequency computations are involved, which easily takes up to an order of magnitude more computation time compared to calculations required for static structures. Additionally, minimum feature size control in topology optimization (through the robust formulation [16]) requires the solution to three different eigenvalue problems in each design iteration, further increasing the computational cost by a factor of three. Ideally, a design with fine resolution can be obtained in a matter of hours.

Validation. Lastly, by actually building and testing a demonstrator, the realized performance of the optimized structure is assessed in reality. This is the ultimate test to see if all practical issues are correctly accounted for and if the optimized performance is as expected.

In this work, we aim to incorporate all aforementioned steps using an industrial case of relevant complexity, from optimization to experimental validation. The main novel contribution is the combination of different aspects required to arrive at a physical industry-relevant product using topology optimization and AM and demonstration of its promised potential. Sub-contributions include (1) the representation of the entire (multi-step) manufacturing process into the optimization in a structured manner, (2) a simple extension of an existing overhang filter [8] significantly improving its geometric accuracy and enabling the use of overhang angles and print directions not aligned with the finite element grid, (3) a novel efficient approach to the robust formulation for eigenfrequency maximization problems [16], reducing the computational cost by a factor three, and (4) experimental validation of an optimized design for a high-tech case study.

This paper is organized as follows. First, Section 2 introduces the industrial design case, which is used as a demonstration for the challenges and optimization process. All aspects of the multi-step manufacturing process are captured into the optimization formulation, and each manufacturing step is explained in detail. In Section 3, an optimized design

is obtained for the case study using the proposed methodology. Its performance is numerically compared with several reference designs and also experimentally validated. Section 4 provides a discussion on the possibilities and limitations of the current work. Finally, concluding remarks can be found in Section 5.

2. Case description and methods

2.1. Chuck optimization case

To help illustrate the challenges and methodology, the design case of a high-precision motion stage is introduced (Fig. 1(a)). This concept can be used, for instance, for the precise positioning of microchips during their production or for their inspection under a microscope. For this application, a high level of precision and repeatability is required as chips consist of many stacked layers with nanometer-sized features and their correct functioning critically depends on connections between the layers. Additionally, this setup is suited for operation in a vacuum environment [17]. A long-stroke stage first provides an extended range of motion with coarse precision. On top of the long-stroke stage, a short-stroke chuck (Fig. 1(b)) is magnetically levitated and its position is actively controlled by a feedback system to provide the required accuracy. This makes the short-stroke chuck the most important component from a system point of view. By designing a chuck with high eigenfrequencies, a high bandwidth can be achieved, which results in higher operating speeds and better accuracy [5]. The goal is therefore to maximize the eigenfrequencies of the short-stroke chuck using topology optimization.

Eight sets of permanent magnets are mounted on the chuck (Fig. 1(b)) and are used for position control in 6 degrees of freedom. The positions of all components are given *a priori* and therefore cannot be changed during the optimization. Two pairs of rectangular magnets are used for in-plane actuation and the four circular magnets are used for out-of-plane actuation and gravity compensation [17]. These are specifically tuned to support a total chuck mass of 18.5 kg. Since 11 kg is used for the magnets (neodymium) and their mounts (stainless steel and aluminum), the remaining 7.5 kg is available for an optimized aluminum frame (AlSi10Mg) produced by the AM process of laser powder-bed fusion.

The outer dimensions of the design domain (excluding components) are $400 \times 400 \times 48$ mm. This both fits in the build-chamber of the MetalFAB1 system of Additive Industries [18] which is used for fabrication, and meets the mass requirement when using 50% of the maximum available volume (*i.e.* volume fraction). To provide sufficient geometric freedom for the optimization, $1 \times 1 \times 1$ mm cubes are used for the parametrization of the design as well as its analysis. The entire chuck including the external components is meshed into a grid of $427 \times 430 \times 49$ elements. Each of these elements has a continuous design-density between 0 (void) and 1 (solid), defined in the design field $\mathbf{x}$. Although the printing process provides a higher resolution than 1 mm, this resolution already results in a formidable computational challenge, as will be discussed in Section 2.2.5.

Optimization problem. For the goal of maximizing a number of eigenfrequencies, effective optimization formulations exist (see, *e.g.*, [13,15]). Following the formulation of Ma et al. [13], objective and constraints are adapted to the problem at hand as

$$
\begin{aligned}
\min_{\mathbf{x}} \quad & \sum_{i=1}^{3} \frac{1}{\omega_i^2} + g_{\text{supp}}, \\
\text{s.t.} \quad & V \leq V_{\text{lim}}, \\
& g_{\text{sol}} \leq 0, \\
& 0 \leq \mathbf{x} \leq 1.
\end{aligned}
\tag{1}
$$

By minimizing the reciprocals of the lowest three eigenfrequencies ω_i, the individual eigenfrequencies are maximized, with focus on the
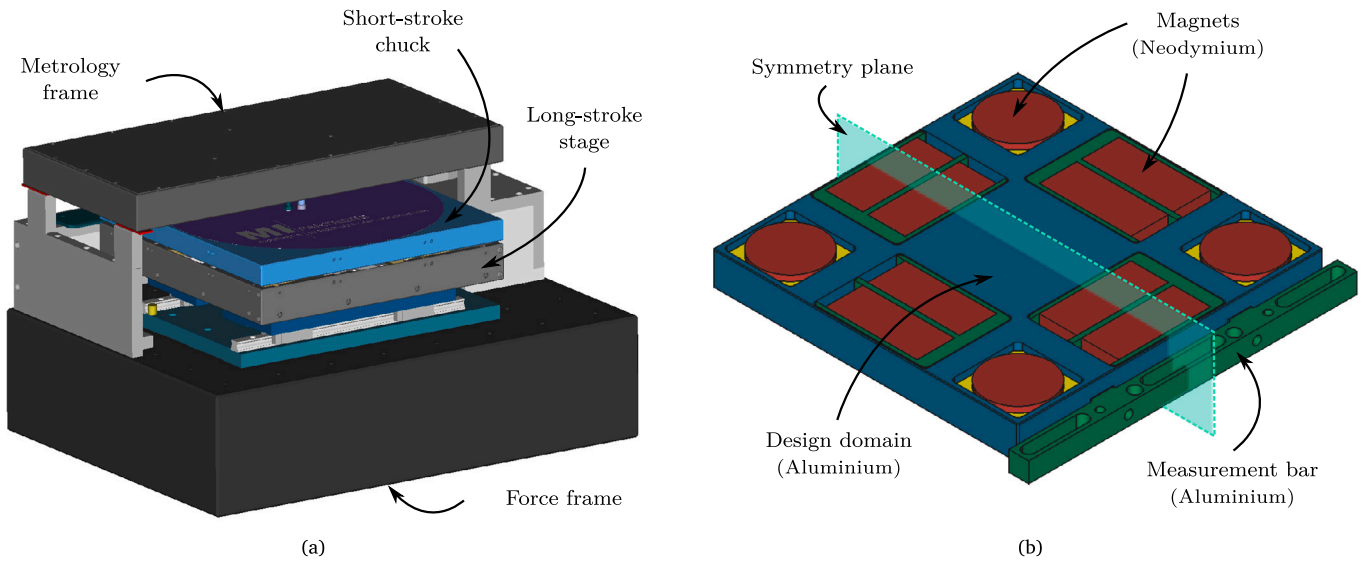
Fig. 1. CAD geometry of the motion stage. (a) Model of the entire stage setup, with the chuck indicated in blue. (b) Bottom view of the chuck showing the design domain for the topology optimization (blue) and required components. The blue and green components are made of aluminum, the yellow of stainless steel, and the red parts are neodymium magnets. Also the plane of symmetry as used in the optimization is indicated. (For interpretation of the references to color in this figure legend, the reader is referred to the web version of this article.)

lowest one. An additional penalty g_{supp} is added to minimize the use of support structures that are removed by milling (Section 2.2.2). This ensures that support material is only added when it is beneficial for higher eigenfrequencies. The design volume V is limited to a maximum of V_{lim}, in order to satisfy the mass requirement. Another constraint g_{sol} is added to enforce sufficient solid material at component interfaces (Section 2.2.1). During optimization, the challenge is to find those design parameters **x** which result in a minimal objective, while satisfying all constraints.

Optimization process. The objective and constraint values need to be evaluated for each design iteration. These depend on the design field **x**, but to ensure a manufacturable design, the design field is passed through a sequence of filters before the calculation of the eigenfrequencies. Each filter accounts for a different aspect towards manufacturability by transforming the design variables, such as enforcing a minimum feature size, removing overhanging features, removing material in milling, or adding the components. A graphical overview of the full filtering and analysis structure can be found in Fig. 2. The series of filters can be seen as a composition of mathematical operators, which transform the initial design field **x** and eventually results in the quantities required for the optimization problem in Eq. (1). All operations in the graph are evaluated from start to end during each design iteration. The individual operations are explained in more detail in Section 2.2.

The design sensitivities (*i.e.* gradients) of the objective and constraints are also calculated during each design iteration, which is required for an effective optimization. The derivations of sensitivities are not discussed in this manuscript, as for all operations they can either trivially be derived, or they can be found in corresponding literature [8,13,16,19]. Once the design sensitivities are available, the design parameters **x** are updated towards an optimal design, using the method of moving asymptotes [20], and the process is repeated until the design stabilizes. Typically 50–150 design iterations are required for an eigenfrequency optimization, depending on the complexity of the optimization formulation.

2.2. Methods

This subsection describes the specific methods involved in the chuck topology optimization scheme outlined in Fig. 2. The large-scale computational process to evaluate the eigenfrequencies is also discussed.

Symmetry. Starting with the first step in the scheme of Fig. 2, which is to convert the design field **x** into a symmetric design **s**. Although a symmetric design is not strictly required, it is preferred to keep the center of gravity close to the midpoint of the chuck, which in this case gives reason to enforce symmetry. A symmetric design is achieved in an element-wise manner, by taking the average of the element density and the density corresponding to the element in its mirror image, mathematically described as

$$s_i = \frac{x_i + x_{n-i}}{2}, \tag{2}$$

where the index i represents the element position in either x, y, or z-direction and n the total number of elements in the corresponding direction. This operation is relatively simple to implement and effectively results in a symmetric density field **s**, which is the average of the design **x** and the design reflected over the chosen plane of symmetry (as indicated in Fig. 1(b)). Additionally, this operation ensures a symmetric distribution of the design sensitivities. In the general case where no symmetry is required in the design, the symmetry step in Fig. 2 can simply be bypassed by setting **s** equal to **x**. The subsequent steps remain identical. Also, multiple planes of symmetry can potentially be introduced.

2.2.1. Additive manufacturing

In order to ensure that the optimized geometry is producible by AM, we apply methods to control the minimum feature size and the maximum overhang angle. Furthermore, assuring the presence of enough material at component interface locations requires a specific constraint. These three measures are discussed in more detail below.

Minimum feature size. The minimum feature size is controlled by applying a projection-based robust formulation in combination with a density filter [16,19]. Next to ensuring a minimum feature size, this method causes the design to become more robust against shape deviations that might occur during printing.

First, as shown in Fig. 2, a length scale is introduced into the design by applying a density filter [19], which is standard practice in topology optimization. This converts the symmetrized design **s** into a smoothed design **d**. Next, by using a projection operator, three designs are produced: a nominal ($\bar{\mathbf{r}}$), an eroded ($\check{\mathbf{r}}$, *i.e.* shrunk), and a dilated
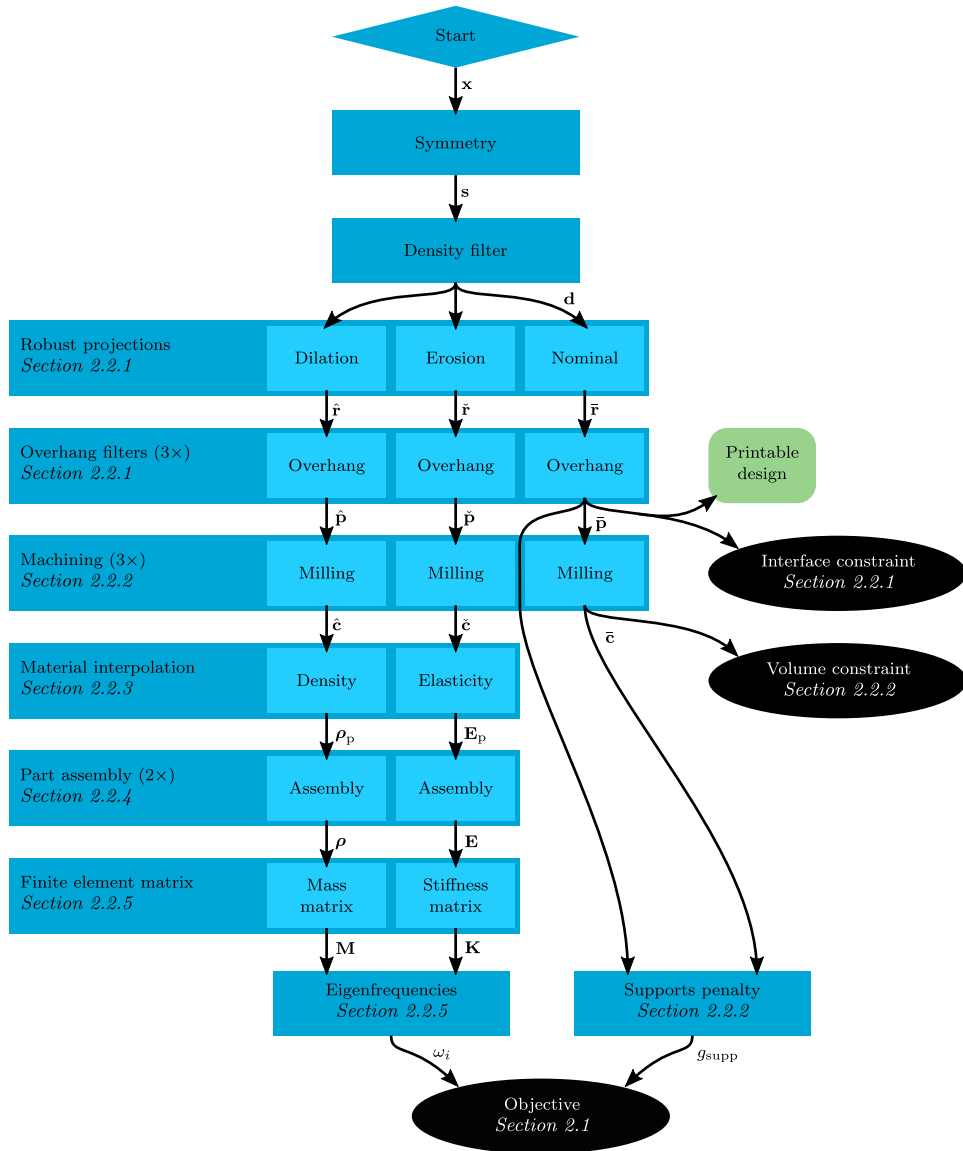
Fig. 2. Graphical overview of the optimization formulation as a flowchart (Eq. (1)). The design variables **x** are passed through a sequence of filters and mathematical operations (the blue blocks) in order to obtain the objective and constraint values (in black) corresponding to a manufacturable design. The entire sequence of operations is executed in each design iteration, where the optimizer repeatedly determines the new design **x**. The design used for actual printing is indicated in green. The individual operations are explained in detail in corresponding sections. (For interpretation of the references to color in this figure legend, the reader is referred to the web version of this article.)
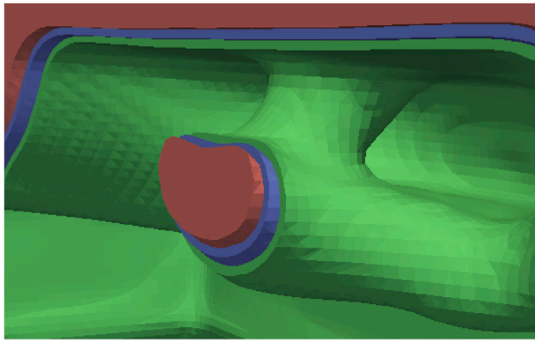

Fig. 3. A cross-section showing the effect of erosion (red) and dilation (green) on the member size. The nominal structure is displayed in blue. (For interpretation of the references to color in this figure legend, the reader is referred to the web version of this article.)

($\hat{\mathbf{r}}$, *i.e.* grown) design, as is shown in Fig. 3. The projection operator is defined as

$$r(d) = \frac{\tanh(\beta\eta) + \tanh(\beta(d - \eta))}{\tanh(\beta\eta) + \tanh(\beta(1 - \eta))}, \tag{3}$$

where β is an intensity factor, and η is the cut-off threshold, which takes different values for the three designs. Together with the density filter, the effective minimum feature size is controlled by the density filter radius r_{filt}, the erosion threshold η_{er}, and the dilation threshold η_{di} [16].

After evaluating the three designs, each will have a different performance. By focusing the optimization on the worst-case scenario (*e.g.* a min–max formulation), the robustness of the final result is improved, and a minimum feature size is obtained [16].

In the case of stiffness maximization, it is intuitive that the eroded design always performs worst, as less material means a lower stiffness [21]. This means that only one finite element solution (that of the eroded design) needs to be calculated, instead of three.

However, the worst-case design is not directly evident when optimizing for maximum eigenfrequencies, since next to the stiffness
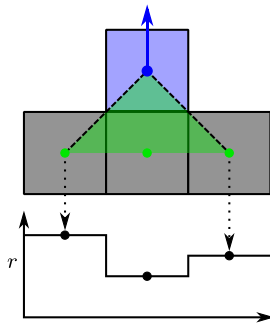
Fig. 4. Illustration of the original sampling scheme in 2D [8], with the graph below showing the element density distribution of the supporting elements. For a vertical print direction (blue arrow), the active element (blue) may be printed if the maximum supporting density is large enough. (For interpretation of the references to color in this figure legend, the reader is referred to the web version of this article.)
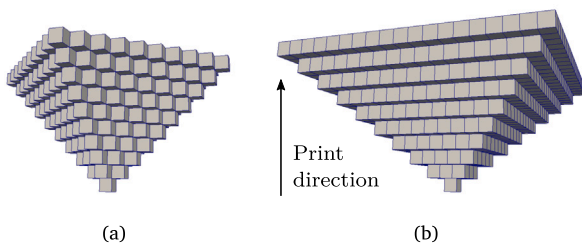

Fig. 5. The printable cone (the largest printable volume, starting from one element) using the original implementation [8], with a 5-element (a) or 9-element support (b).

distribution, the mass distribution also plays an important role. In order to avoid calculating the eigenfrequencies three times, we use an adapted worst-case scenario: the mass-field ρ is dilated (always more mass) and the stiffness-field $\mathbf{E}$ is eroded (always less stiffness), as is indicated in the diagram of Fig. 2. Using these settings, a single solution of the eigenvalue problem results in worst-case eigenfrequencies, which are lower than in the nominal case (proof is provided in Appendix). These values are used in the objective function of Eq. (1).

Overhang limitation. To ensure a maximum overhang angle in the design,[1] an overhang filter is used. Effectively, it converts the projected design $\mathbf{r}$ to a printable design $\mathbf{p}$ (Fig. 2) by removing all features overhanging beyond a critical angle. In this case, all three designs are filtered, resulting in three printable designs (nominal $\bar{\mathbf{p}}$, eroded $\check{\mathbf{p}}$, and dilated $\hat{\mathbf{p}}$). Note that the combination of the robust method with an overhang filter affects the effective minimum feature size, which could be corrected using more elaborate formulations [22]. Naturally, the nominal design $\bar{\mathbf{p}}$ serves as the printable design used for actually printing the part, as indicated by the green box in Fig. 2.

The overhang filter as proposed by Langelaar [8] proceeds layer-wise through the structure and determines the maximum printable density of each element in the layer, which is used as a threshold to limit the original density. The maximum printable density is determined by taking the maximum value of the supporting elements below the current element (3 elements in 2D as illustrated in Fig. 4, and 5 or 9 in 3D as seen in Fig. 5).

Because in the original formulation discrete elements are used as supports, the effective maximum overhang angle is non-uniform and dependent on the alignment with the Cartesian coordinate system of the mesh [8]. Ideally, a printable cone has an axisymmetric maximum
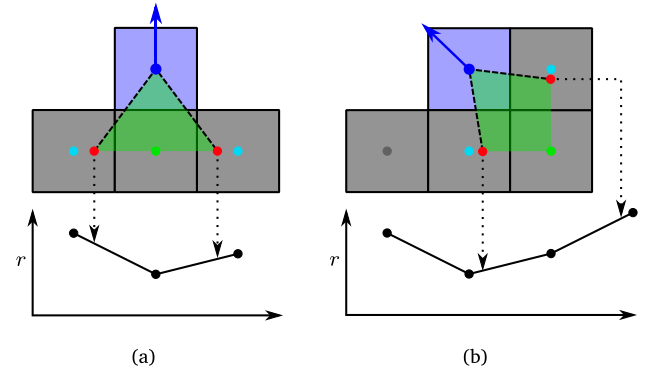

Fig. 6. The improved sampling scheme in 2D. (a) An overhang angle smaller than 45° uses one element midpoint (green) and two interpolation points (red) below the active element (blue) as support. (b) A diagonal print direction, where one sampling point interpolates between the two elements to the right of the active element. Elements indicated with cyan are used only in interpolation. The horizontal axis of the density graph is wrapped around the corner. (For interpretation of the references to color in this figure legend, the reader is referred to the web version of this article.)

overhang angle around the print direction, independent on the mesh. When using 5 support elements, the printable cone is pyramid-shaped (Fig. 5(a)), which is conservative in the off-axis directions with an effective overhang angle of 35° on a cubical mesh. The version with 9 support elements on the other hand shows the opposite behavior, being less restrictive in off-axis directions with an overhang of 55°, which violates the required maximum overhang angle (Fig. 5(b)). Additionally, these sampling patterns only allow overhang angles of 45° (in case of a cubical mesh), at print-directions aligned with the Cartesian coordinate system of the mesh. Various other overhang prevention approaches have been proposed, e.g. [7,9,10,12], each differing in effectiveness, complexity, and convergence characteristics.

Here we propose a comparatively simple yet effective improved scheme that still benefits from the regularity of the structured mesh, but reduces the dependency on the mesh. It enables a more accurate geometric description of the maximum overhang angle and additionally enables an arbitrary print direction and a maximum overhang angle other than 45°. To do this, interpolation is used to sample densities at locations that do not exactly coincide with an element midpoint (Fig. 6(a)). In 2D, a triangle is projected onto the supporting plane, which is the plane passing through the midpoints of the supporting elements. The current element may be printed if the maximum density within the supporting area is large enough. This maximum is located either on one of the element midpoints within the cone or at the boundary, for which linear interpolation is used.[2] By changing the opening angle of the projecting triangle, the maximum overhang angle can be controlled. A rotation of the triangle results in a change of print direction, as is illustrated in Fig. 6(b). For this case, elements adjacent to the current element are used for the rotated case, making the supporting surface fold around the corner.

In 3D, the supporting area is determined by a cone instead of a triangle, as demonstrated in Fig. 7. The allowable overhang angle is controlled by the aperture of the cone, and the print direction by its orientation. Just like the two-dimensional case, the maximum printable density is found at one of the element midpoints within the cone or at the perimeter of the cone. A number of equally spaced sampling points is defined along the perimeter, approximating the density value at those locations using bilinear interpolation based on the density values of the four closest elements. The weights used for the bilinear interpolation

---

[1] Maximum overhang angle as measured from the normal to the buildplate.

[2] This is only assumed for densities in the overhang filter. For each element in the finite element analysis, its material density is constant throughout.
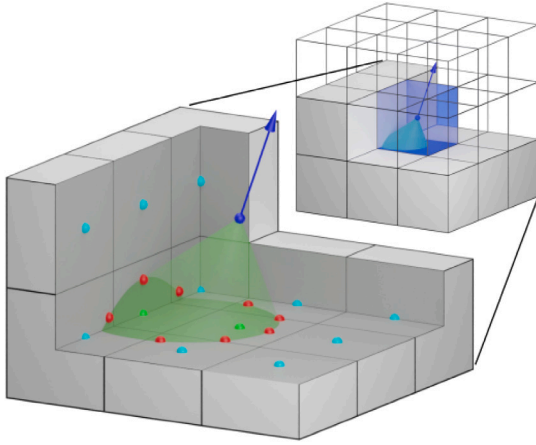
Fig. 7. The improved sampling strategy with an arbitrary print orientation, indicated by the blue arrow. The maximum printable density of the active element (in blue) is determined by the elements in the direction of the support cone (green). A combination of densities within the cone obtained directly at element midpoint (2x green dots), and interpolated values along the perimeter of the cone (8x red dots) are used in a smooth maximum function. (For interpretation of the references to color in this figure legend, the reader is referred to the web version of this article.)

can be precomputed since a structured grid is used, thus ensuring a computationally efficient overhang filter.

The maximum printable density is now obtained by taking a smooth maximum of both the values at element midpoints encompassed by the cone and the sampled points along the perimeter of the projected cone. Instead of 5 or 9 points, this results in a variable number of points, depending on print orientation, maximum overhang angle, and chosen number of perimeter points. The final step in the overhang filter is to take a smooth minimum of the original density of the current element and the maximum printable density, which is identical to that of the original implementation [8].

The printable cone converges to a circular shaped cone by increasing the number of sampling points, as is demonstrated in Figs. 8(a) and 8(b), correcting the under- and over-estimation as observed in the original 5 or 9 element support (Fig. 5). Using the improved method, also overhang angles smaller than 45° (narrow support cones, Fig. 8(c)) can easily be modeled by simply adapting the shape of the supporting cone, thus sampling at different locations. Additionally, arbitrary printing orientations are enabled by rotating the supporting cone (Fig. 8(d)), instead of requiring domain mapping [23]. Also other support patterns, *e.g.*, elliptic cones, are a natural extension to the method.

Note that in order for this refined overhang filter to work correctly, only processed elements are allowed to be accessed. This can be ensured by changing the element traversal pattern, depending on the print direction. In general, for overhang angles above 45° it becomes much more difficult or even impossible to obtain a traversal pattern that ensures all sampled elements are processed. A critical overhang angle of 45° is used for the present study , for which the proposed overhang filter is used for an improved geometric accuracy of the maximum overhang limitation.

Enforcing interfaces. For the assembly of the different components to the printed body, interfaces for bolts need to be generated. This is not evident in the optimization, because there is no incentive to connect the bodies other than for stiffness. In practice, sufficient material is required at bolt locations for a hole to be drilled and threaded, as is illustrated in Fig. 9. Only setting the required volume to solid (*i.e.* frozen/non-design area) does not ensure printability of these locations, and they may even be removed by the overhang filter. Therefore, sufficient material is forced at the bolt locations by using an additional constraint [24], as is depicted in Fig. 2. This is done by taking the root

sum of squares for the differences between the density values of the nominal printable design $\bar{\mathbf{p}}$ and their desired value (in this case 1.0), denoted in a formula as

$$g_{\text{sol}} = \frac{1}{N_{\mathcal{F}}} \sqrt{\sum_{i \in \mathcal{F}} (1.0 - \bar{p}_i)^2} - \tau \leq 0. \tag{4}$$

The set of elements marked to be solid is denoted $\mathcal{F}$, the number of elements in this set $N_{\mathcal{F}}$, and a small tolerance value τ is used to allow some slack. In this manner, the optimization process will not only ensure the presence of material at these bolt regions, but also its printability.

2.2.2. Milling

The next step in the (simulated) production process is milling (Fig. 2). After obtaining a printable design, pockets are cleared of support structures, as indicated in Fig. 10, where components are to be mounted. Here, by support structures we mean the material that is required for a printable design, but is removed in the milling step. Any support structures generated outside of the milled volume are not removed and are considered a part of the final structure. Adaptive formulations for topology optimization also exist, where support structures (not in benefit to the final performance) are identified and removed throughout the domain, instead of only in a pre-determined volume [24,25]. However, this is not incorporated in the current work.

Mathematically, the milling operation is done by taking the printable designs ($\bar{\mathbf{p}}$, $\check{\mathbf{p}}$, and $\hat{\mathbf{p}}$) and setting the entries corresponding to the milled volume to zero as

$$c_i = \begin{cases} 0 & \forall \quad i \in \mathcal{M} \\ p_i & \forall \quad i \notin \mathcal{M} \end{cases} \tag{5}$$

where c_i are the entries in design vectors $\bar{\mathbf{c}}$, $\check{\mathbf{c}}$, and $\hat{\mathbf{c}}$, denoting the milled designs and $\mathcal{M}$ represents the elements in the milled volume, which are known *a priori*. Note that in this case, no tool access restrictions are involved, since the relevant pockets are always accessible from the base of the chuck. A more complex milling formulation, such as in [26], is therefore not required in this case.

As mentioned in Section 2.1, the required mass of the unassembled chuck is $M_{\text{lim}} = 7.5\,\text{kg}$, for which a constraint can be formed at this point (Fig. 2). By a simple addition, the volume of the machined chuck frame can be calculated as

$$V = \sum_i \bar{c}_i V_{\text{e}}, \tag{6}$$

with V_{e} the volume of one element. The volume limit V_{lim} is calculated as

$$V_{\text{lim}} = \frac{M_{\text{lim}}}{\rho_{\text{alu}}}, \tag{7}$$

with material density ρ_{alu}. Strictly speaking, the volume constraint should be an equality constraint, but since the upper bound is generally active, it can be reduced to an inequality constraint, which is easier to implement in the optimization (Eq. (1)).

Support structure minimization. Since the milled field is used for the volume constraint instead of the printed field, the use of support structures is unbounded, which may lead to excessive material use during the print process. This effect is counteracted by adding a penalty on the volume of removed support structures, keeping the amount of support material to a minimum. The volume of the cleared support structures can simply be calculated from the difference between the nominal printed volume and the volume after milling V (Eq. (6)) as

$$V_{\text{supp}} = V_{\text{print}} - V \, , \text{ with } \quad V_{\text{print}} = \sum_i \bar{p}_i V_{\text{e}}. \tag{8}$$

This value is added to the objective in Eq. (1) as a penalty value (Fig. 2)

$$g_{\text{supp}} = \alpha \frac{V_{\text{supp}}}{N_{\mathcal{M}}}, \tag{9}$$
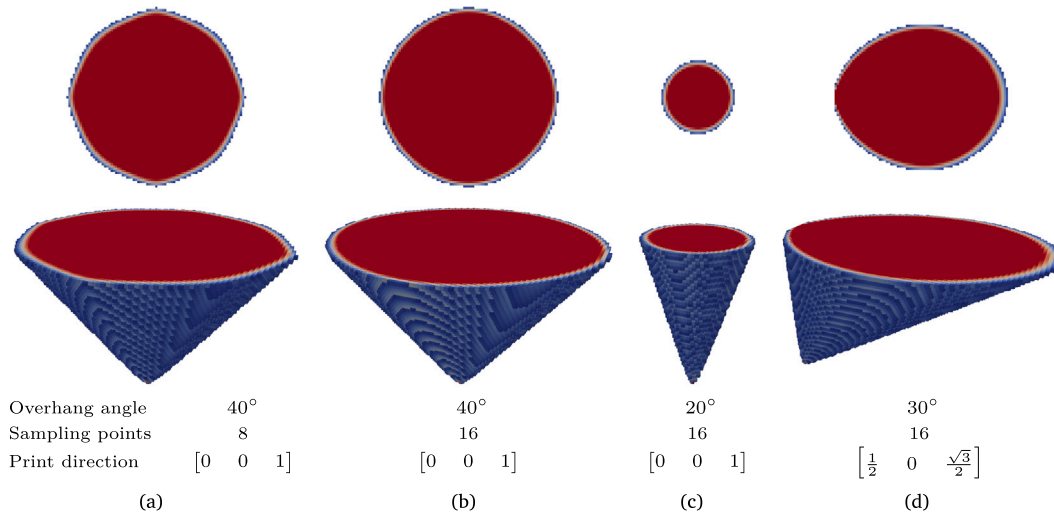
Fig. 8. The printable cone using different number of sampling points, overhang angle, and orientation, but using the same mesh. The top row shows the top view, and in the bottom row, the perspective view is displayed.
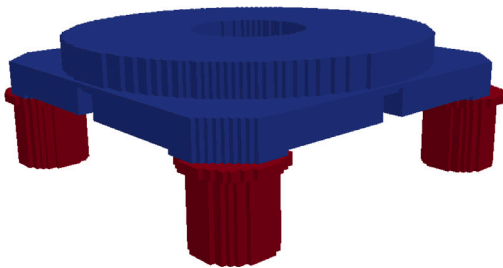

Fig. 9. One of the magnets (blue), and in red the cylindrical interface volumes large enough for a threaded and bolted connection. (For interpretation of the references to color in this figure legend, the reader is referred to the web version of this article.)
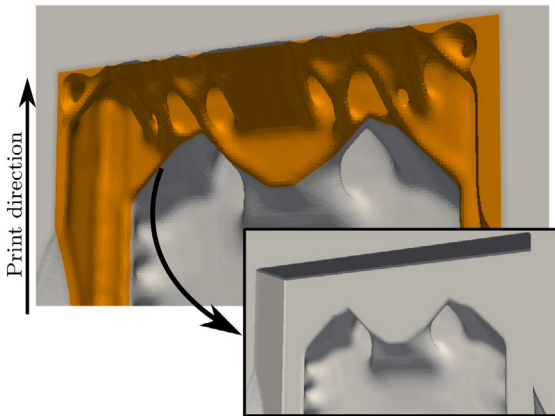

Fig. 10. A detailed view of support structures (indicated in yellow), which are removed by the milling operation. Supports are required to print the upper side wall of the actuator pocket, and therefore these structures are generated in the optimization process. (For interpretation of the references to color in this figure legend, the reader is referred to the web version of this article.)

where the volume is normalized using the number of elements marked for milling $N_{\mathcal{M}}$, and α is a small penalty factor that determines how much focus is on limiting the amount of support structure. This causes support structures to appear only when they are effective in supporting material beneficial for higher eigenfrequencies. A detail of a resulting structure can be seen in Fig. 10.

2.2.3. Material interpolation

The material properties of the chuck's milled body are a function of density field **c**, as can be seen in Fig. 2. They are interpolated using SIMP (Solid Isotropic Microstructure with Penalization), which is a standard method in topology optimization [6]. This enforces a penalization on intermediate design variables (neither 0 or 1), and helps the optimization process to converge towards an interpretable black-and-white design. In eigenfrequency optimization often problems are encountered with localized eigenmodes in low-density areas ($c \approx 0$) and their low corresponding frequencies. To alleviate these problems we use the approach proposed by Zhu et al. [27], where a small linear part is added to the usual cubic power of SIMP (Eq. (10)). This prevents the stiffness from vanishing as compared to the mass for very small densities c. The stiffness $\mathbf{E}_{\mathrm{p}}$ and mass ρ_{p} distribution of the printed and milled part can be calculated using the eroded $\check{\mathbf{c}}$ and dilated $\hat{\mathbf{c}}$ density fields, respectively, as

$$E_{\mathrm{p},i} = E_{\mathrm{alu}} \left(c_{\min} + \left(1 - c_{\min} \right) \left(0.1 \check{c}_i + 0.9 \check{c}_i^3 \right) \right),$$
$$\rho_{\mathrm{p},i} = \rho_{\mathrm{alu}} \hat{c}_i, \tag{10}$$

where a minimum design variable $c_{\min}$ prevents the stiffness matrix from becoming (more) singular. In the current design case the system matrix is already singular because of rigid-body-modes, but these modes are known analytically and accounted for, as is explained in Section 2.2.5.

2.2.4. Component assembly

At this point the distribution of density and elasticity modulus is known throughout the milled product, and the components (magnets and measurement bar) can be added (Fig. 2). Similar to the milling operation, this is done by setting the entries in the final material properties (**E** and ρ) to either that of the milled part or to that of the components as

$$E_i = \begin{cases} E_{\mathrm{c},j} & \forall \quad i \in C_j \\ E_{\mathrm{p},i} & \forall \quad i \notin \bigcup_j C_j \end{cases} \tag{11}$$

and

$$\rho_i = \begin{cases} \rho_{\mathrm{c},j} & \forall \quad i \in C_j \\ \rho_{\mathrm{p},i} & \forall \quad i \notin \bigcup_j C_j, \end{cases} \tag{12}$$

where $E_{\mathrm{c},j}$ and $\rho_{\mathrm{c},j}$ denote the modulus of elasticity and density for each component with elements C_j.

Bolted interfaces are modeled by connecting two components with a patch of solid material (Fig. 11). Since all components are modeled in the same mesh, the connecting patch is 1 element thick. The diameter
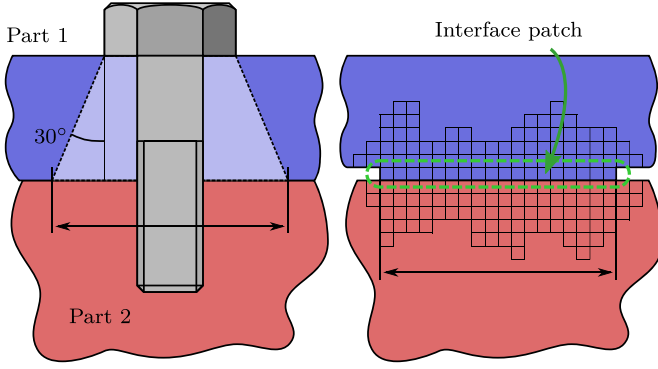
Fig. 11. A bolted interface with indicated frustum, used to determine the patch diameter (left). The two discretized parts are connected by a solid patch of 1 element thickness (right).

of the patch is calculated according to a 30° frustum starting at the bolt head, corresponding to the pressure cone of the bolt [28]. In this way the bolts are modeled in an effective, yet simple manner.

Geometry mapping. The CAD geometry of the magnetic actuators is converted to a 3-dimensional structured grid (voxel grid) by using a rasterizing algorithm, also called solid voxelization. Effectively, this means that all the elements of which the center-point is inside the solid CAD geometry are detected, and placed into the sets C_j representing the different components. The result of this operation can be seen in Fig. 12.

The voxelization is implemented as a simple scanline algorithm (see, *e.g.*, [29]) in three dimensions. Rays are cast in each axis-aligned direction, through the center of each element in the mesh. For each ray, intersection with the geometry is tested, which generally results in one or multiple pairs of entry–exit intersections. When an element is within an intersected range of all three the x, y, and z-directions, its center is inside the geometry and thus can be marked as part of the considered geometry set C_j. This process only needs to be done once, prior to the optimization.

2.2.5. Finite element modeling

The entire domain is discretized into a grid of trilinear hexahedral solid elements with a full integration scheme and dimensions $1 \times 1 \times 1$ mm, corresponding to the design resolution. For each of the elements, the material properties associated with the respective
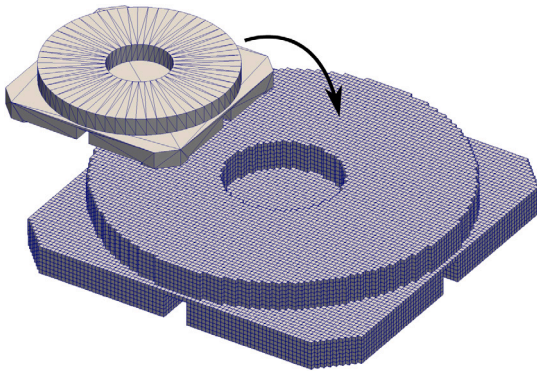

Fig. 12. An example of voxelization, where the original boundary representation of a magnet and its mount (top left) is mapped onto a 1 mm grid (bottom right).

components and/or optimization variables have been determined by the preceding steps shown in Fig. 2, where the (penalized) Young's modulus **E** and the mass density ρ depend on the eroded $\check{\mathbf{c}}$ and dilated $\hat{\mathbf{c}}$ design fields, respectively (Eqs. (10)–(12)). Following standard topology optimization procedure, the stiffness **K** and mass **M** matrices can be constructed by linear scaling of each element i with the material properties E_i and ρ_i as

$$\mathbf{K} = \bigwedge_i^{N_{\mathrm{el}}} E_i \mathbf{K}_0 \quad \text{and} \quad \mathbf{M} = \bigwedge_i^{N_{\mathrm{el}}} \rho_i \mathbf{M}_0, \tag{13}$$

where $\mathbf{K}_0$ and $\mathbf{M}_0$ represent the unit stiffness and mass element matrix, and the operator $\mathbb{A}$ represents the matrix assembly. The two element matrices are identical throughout the domain, since a structured mesh of equal-sized elements is used.

After assembly, the next step in Fig. 2 is to calculate the eigenfrequencies. The three eigenfrequencies are found as solutions to the generalized eigenvalue problem, denoted as

$$(\mathbf{K} - \omega_i^2 \mathbf{M}) \boldsymbol{\varphi}_i = \mathbf{0} \quad \text{for } i = 1, 2, 3$$
$$0 < \omega_1 \leq \omega_2 \leq \omega_3, \tag{14}$$

where ω_i and $\boldsymbol{\varphi}_i$ are the structural eigenfrequencies and their corresponding eigenvectors. The entire analysis domain (including all components) consists of a total of 9.0 million elements, and 27.6 million degrees of freedom. This very large number of degrees of freedom poses a computational challenge, especially because calculating a single eigenfrequency is already an order of magnitude more expensive than the solution of a static response.

For an efficient solution, we resort to parallelization of the problem. The finite element routines are implemented using the PETSc library [30], which provides parallel linear solvers, data structures for parallelization, and domain decomposition. For the solution of the eigenfrequencies (Eq. (14)), specialized eigensolvers are used from the SLEPc library [31], which is an add-on to PETSc. A Krylov–Schur algorithm with a shift-and-invert strategy is used to obtain the three lowest eigenfrequencies ω_i and corresponding eigenvectors $\boldsymbol{\varphi}_i$. In the calculation of eigenvalues, the repeated solution to a large linear system of equations is required, for which we use the iterative Stabilized BiConjugate-Gradient (BiCGStab) method, preconditioned with an algebraic multigrid preconditioner.

Since the motion stage is free-floating, no boundary conditions are present, making the stiffness matrix singular. To prevent numerical problems in the solvers, deflation is used to account for the six rigid body modes (*i.e.* nullspace) in both the eigensolver and its internal linear solver. The deflation ensures a solvable linear system of equations and prevents recomputation of the rigid body modes, which are already known explicitly [32]. Further details on the aforementioned algorithms can be found in the PETSc and SLEPc documentation [30, 31].

2.2.6. Settings

All settings as used in the optimization can be found in Table 1. To help convergence, the first few iterations the overhang filter is not active, but is gradually phased in during iterations 15–65, reducing the aggressiveness of this filter (similar approach as in [12]). Also the robustness factor β is gradually increased during the optimization process in iterations 10–90. The chosen filter radius and erosion/dilation thresholds result in an effective minimum feature size of $2r_{\mathrm{filt}}\sqrt{\eta_{\mathrm{er}} - 0.5} \approx 3.2$ mm, according to [33].
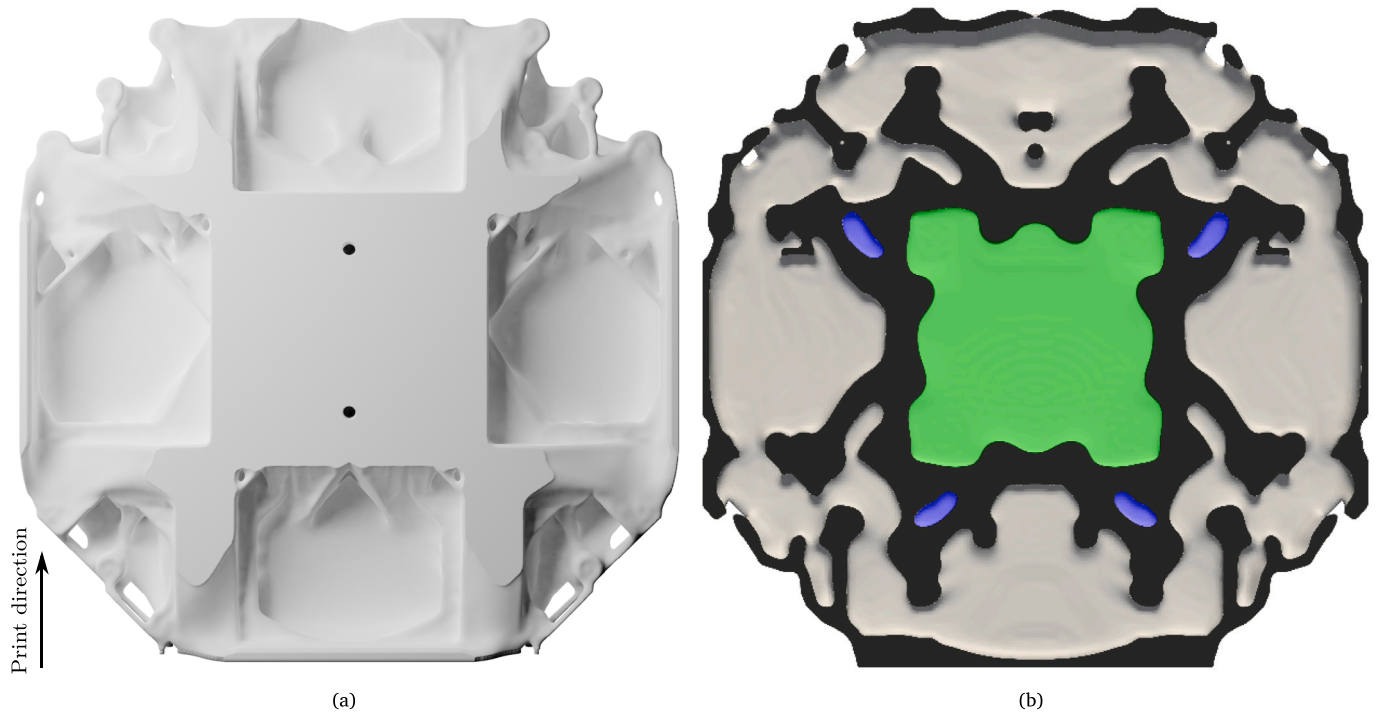
(a)

(b)

Fig. 13. (a) The (printable) geometry of the optimized chuck. b) Cross-section of the geometry, showing the internal structure of the chuck. Several small enclosed voids are removed (blue) and for the large cavity in the middle (green), extra holes are added to allow powder evacuation. (For interpretation of the references to color in this figure legend, the reader is referred to the web version of this article.)

Table 1
Options and settings as used in the optimization.

| Symb.	Value	Description
E_{alu}	65 GPa	Young's modulus (aluminum)
ρ_{alu}	2700 kg/m³	Density (aluminum)
E_{neo}	160 GPa	Young's modulus (neodymium)
ρ_{neo}	7500 kg/m³	Density (neodymium)
E_{ss}	200 GPa	Young's modulus (stainless steel)
ρ_{ss}	8000 kg/m³	Density (stainless steel)
ν	0.3	Poisson's ratio (all materials)
c_{min}	10^{-5}	Minimum density
r_{filt}	5 mm	Filter radius
η_{er}	0.6	Erosion threshold
η_{di}	0.4	Dilation threshold
β	$10^{-9} - 10^{1}$	Projection intensity factor
	45°	Overhang angle
	8	Overhang sampling points
τ	10^{-5}	Solid constraint tolerance
α	10^{-6}	Support structure penalty factor
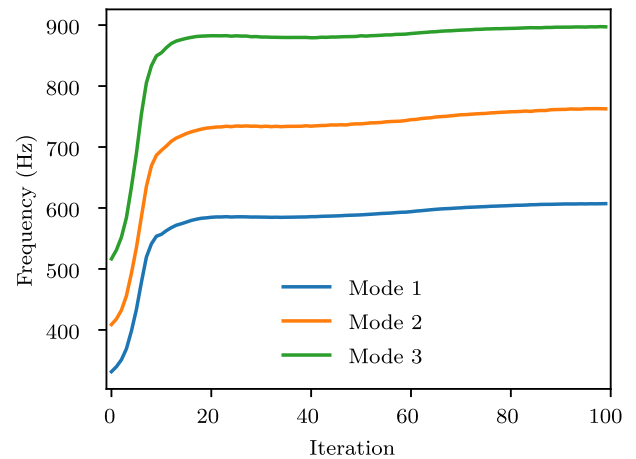
Fig. 14. Iteration history of the eigenfrequencies.

3. Demonstrator and experimental validation

3.1. Optimized design

After the optimization, a final geometry is obtained as shown in Fig. 13(a). This geometry is the iso-surface of the voxel grid of the nominal printable design $\bar{\mathbf{p}}$ at a density value of 0.5. The iso-surface can be generated using the marching cubes algorithm, which is implemented in, *e.g.*, the open source visualization application Paraview [34]. Low resolution versions of the 3D model are included in the supplementary material. The support structures and required volumes for component interfaces can clearly be identified. Fig. 13(b) shows the internal structure of the chuck. The final geometry contains several enclosed voids, which were not accounted for during the optimization. To prevent trapped metal powder, the enclosed voids are removed by manual post-processing. Four small voids were converted to solid

material, and for the large void in the center, two holes were added for powder removal after printing, as indicated in Fig. 13(b).

The evolution of the eigenfrequencies throughout the optimization is shown in Fig. 14, from which can be seen that the final frequencies are 607, 763, and 897 Hz. However, these values refer to the robust worst-case design (Section 2.2.1). From a verification analysis on the nominal design, we find the expected eigenfrequencies as 667, 837, and 1011 Hz. The corresponding mode shapes (Fig. 15) are as expected from a fairly flat plate; a torsional, saddle, and umbrella mode.

To ensure a minimum length scale, the design is uniformly perturbed in order to obtain worst-case eigenfrequencies. In Section 2.2.1 is explained that using an eroded design for the stiffness and a dilated design for the mass leads to lower eigenfrequencies. This effect is shown in Fig. 16(a), where the first five eigenfrequencies of the final design
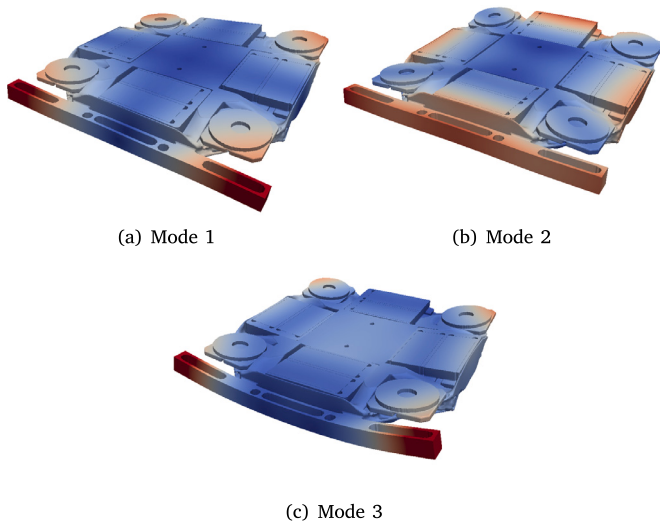
(a) Mode 1   (b) Mode 2

(c) Mode 3

Fig. 15. (a) The first eigenmode at 667 Hz (torsion mode). (b) Second eigenmode at 837 Hz (saddle mode). (c) Third eigenmode at 1011 Hz (umbrella mode).

Fig. 17. Detail of the printable structure, which is optimized using the improved overhang filter. Areas indicated in red are not allowed using the original overhang filter with the conservative 5-element support. (For interpretation of the references to color in this figure legend, the reader is referred to the web version of this article.)

(a)   (b)

Fig. 18. (a) Solid reference design, with equal mass or equal height. (b) Conventional reference design, with equal mass and equal height.

are calculated with different thresholds of erosion $\eta_{er} = 0.5 + \Delta\eta$ and dilation $\eta_{di} = 0.5 - \Delta\eta$. The offset in mass and stiffness becomes larger for increasing $\Delta\eta$, leading to lower eigenfrequencies. However, for values above $\Delta\eta \approx 0.2$ the eigenfrequencies drop significantly due to localized eigenmodes. The first eigenmode at $\Delta\eta = 0.3$ is shown in Fig. 16(b), where a localized deformation can clearly be recognized. Using an excessively large offset ($\Delta\eta$) between mass and stiffness thus causes undesired spurious modes. For the current optimization $\Delta\eta = 0.1$ is used, which does not cause localized eigenmodes.

An improved overhang filter has been presented in , which enables a more geometrically accurate description of overhang. A detail of the final optimized structure is shown in Fig. 17, with several areas indicated which would be removed by the original overhang filter with a 5-element support, which is too conservative [8]. This demonstrates the added value of the improved geometric accuracy of the overhang filter.

To get an indication of the optimized performance relative to other designs, three reference cases are established. The first two reference designs use a 100% material inside the design domain (Fig. 18(a)). Since the chuck is originally optimized with a volume fraction of 50%, the mass of a completely solid chuck will double. Therefore, the first reference has equal height to the optimized chuck, but doubled mass.
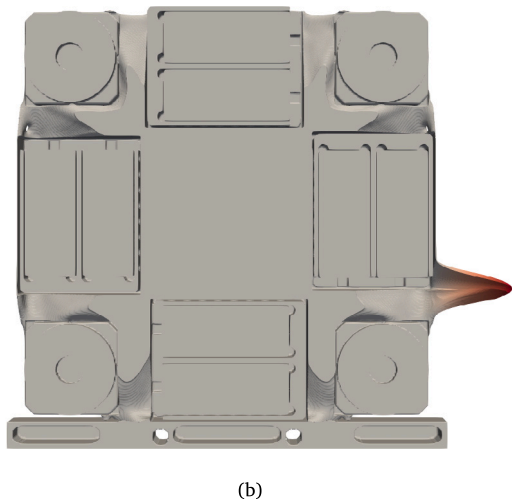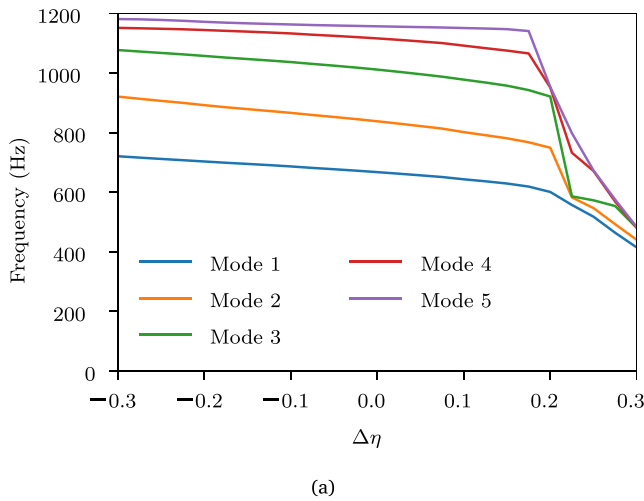

(a)

(b)

Fig. 16. (a) The eigenfrequencies as a function of the Heaviside threshold parameter. The stiffness matrix is obtained with $\eta_{er} = 0.5 + \Delta\eta$ and the mass matrix with $\eta_{di} = 0.5 - \Delta\eta$. (b) The first eigenmode at $\Delta\eta = 0.3$ contains a localized deformation. This spurious eigenmode is caused by the large offset in the eroded and dilated design.
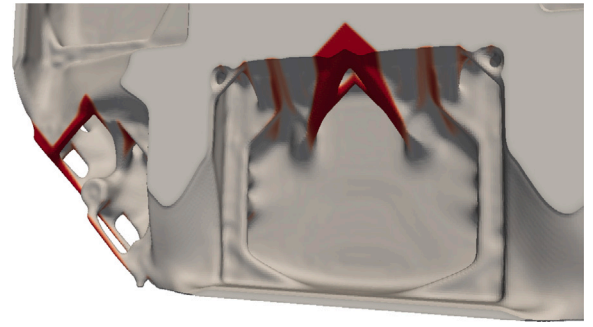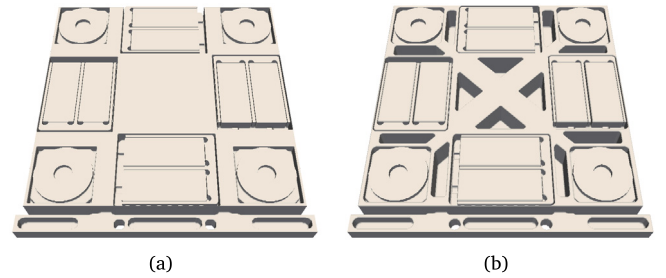
Table 2
Results of the numerical comparison between optimized and reference designs.

	Units	Optimized	Reference designs					
			Equal mass		Equal height		Conventional	
Mass[a]	kg	7.5	7.5		15		7.5	
Height	mm	48	30		48		48	
Mode 1	Hz	667	353	−47%	569	−15%	547	−18%
Mode 2	Hz	837	414	−51%	815	−2.6%	735	−12%
Mode 3	Hz	1011	525	−48%	944	−6.6%	880	−13%

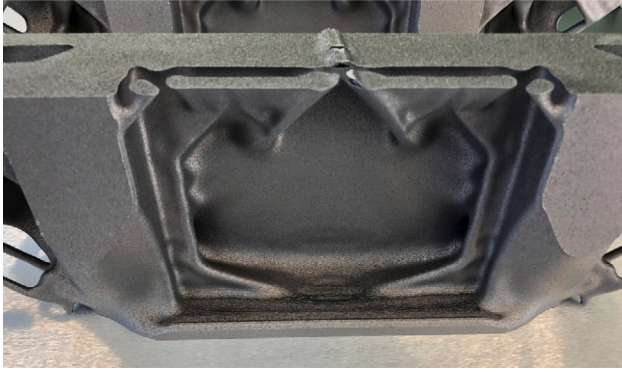[a]Mass of the machined part only, excluding any components.

Fig. 19. The first print attempt, showing the locally overheated and deformed parts, causing recoater damage.

In the second reference design, the height of the chuck is reduced such that the mass is equal to that of the optimized design. And thirdly, a conventional and manually designed chuck (with equal mass and dimensions to the optimized design) is analyzed (Fig. 18(b)). An overview of the results for these variations can be found in Table 2. The optimized design clearly outperforms all reference chucks. With respect to solid designs, the performance is roughly doubled, or the mass can significantly be reduced while still increasing performance. When compared to a conventional and manually designed chuck, also a considerable performance increase of about 15% can be realized.

In terms of computational time, the entire optimization took 25 h. This means that each of the 100 design iterations which were performed, requires an average of 15 min. The computations were executed on a 192-core computing node (8× Intel Xeon 8168 24-core CPU and 1536 GB of memory). About 400 GB is required for the optimization out of the total available memory.

3.2. Additive manufacturing

For larger and complex designs, the part orientation in the build chamber is the key element for successful printing. Since print orientation is fixed throughout the optimization, several part orientations have been analyzed prior to the optimization. Finally, it was chosen to orient the part vertically for minimal stress in the horizontal plane, to limit the amount of support structures required, and for an easy part separation from the buildplate. The disadvantage of this approach is the need to use the full build height, the initial powder investment, and longer job duration due to the recoater time. However, this is offset by the opportunity to print multiple parts simultaneously (up to 4 in one job) and allowing the use of multiple lasers in the MetalFAB1 system [18]. No extra support structures nor any further adaptations to the design were required, as the overhang filter enforces a self-supported design (Section 2.2.1).

The first print was halted due to too large heat accumulation at the connection of two overhanging areas. Locally melted material protruded above the powder bed, resulting in recoater damage (see Fig. 19). Incorporation of a process-based simulation of the printing process into the optimization can potentially avoid these kind of failures, and help in obtaining a first-time-right print, although its computational feasibility is currently out of reach for the design resolution targeted in this study [35]. After reorienting the parts with respect to the recoater, the build job ran smoothly over the full part height (Fig. 20). The selected print parameter settings are balancing productivity (30 µm layer thickness) and density, resulting in an 'as printed' density above 99.95% (from cross-sectional analysis) of the
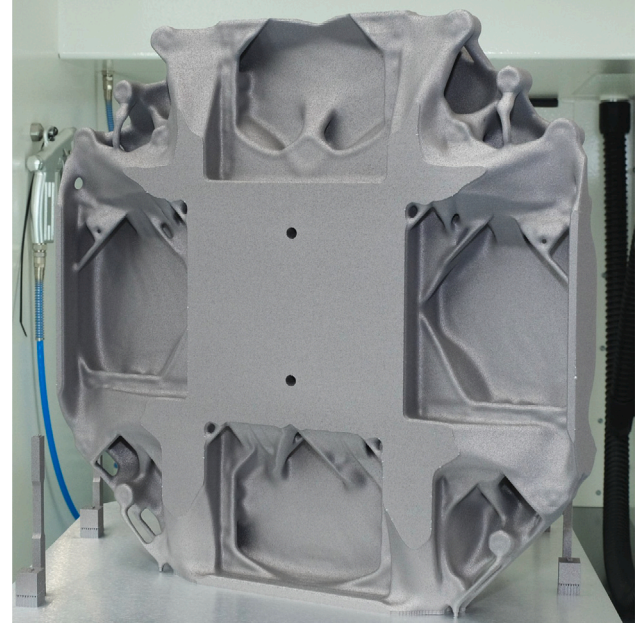

Fig. 20. The printed chuck after the powder-bed fusion process is finished.
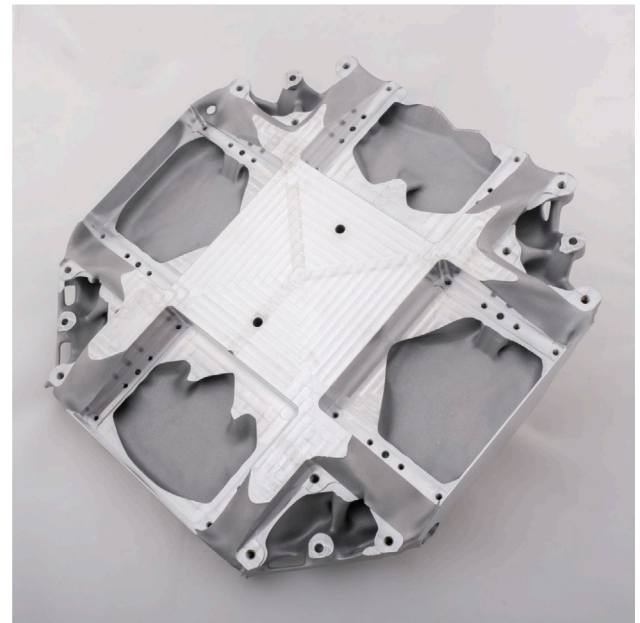

Fig. 21. After machining, support structures are removed and interfaces for the components added.

AlSi10Mg material. Two parts were printed simultaneously in a total of 10 days, effectively resulting in 5 days build time per part.

In order to achieve surface and dimensional requirements for the interfaces of all the magnets which cannot be achieved by the printing process, the part is post-processed by traditional machining methods (Fig. 21). The final step is to assemble the magnets and mount the chuck on the long-stroke chuck, making it ready for usage (Fig. 22).
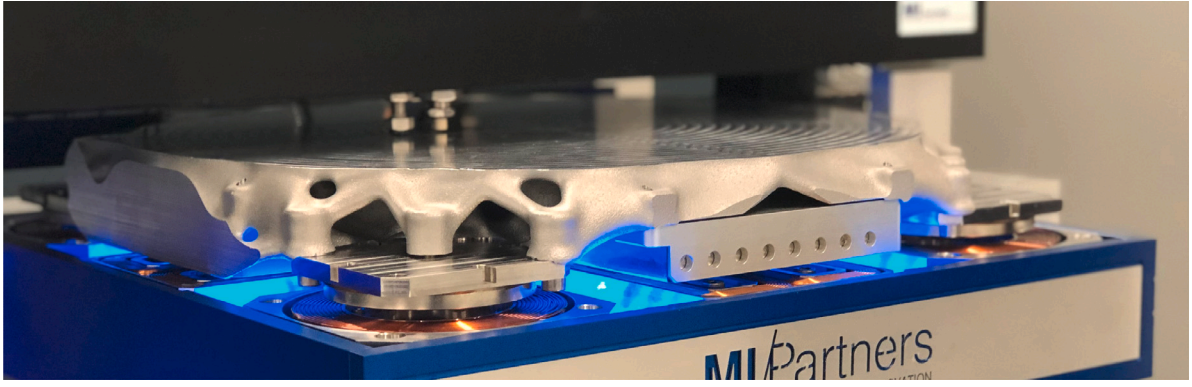
Fig. 22. Assembled chuck in operation, levitated above the long-stroke stage.

3.3. Validation

The chuck position in all six degrees of freedom is actively controlled by a closed-loop feedback loop, which can be used for a frequency-response measurement (Fig. 23). Five eddy current sensors and one laser interferometer provide position measurement of the chuck, and eight (sets of) permanent magnets are able to apply forces on the chuck when placed in magnetic fields generated by external voice coils (Fig. 1). A force or moment can be applied on the different degrees of freedom of the chuck $\mathbf{f}_{\mathrm{act}}(t) = [F_x, F_y, F_z, M_x, M_y, M_z]$ by applying a load on multiple actuators simultaneously. Similarly, displacements in global degrees of freedom $\mathbf{u}_{\mathrm{sens}}(t) = [U_x, U_y, U_z, \theta_x, \theta_y, \theta_z]$ (translations or rotations) are obtained by a linear combination of the different sensor signals. Further details on sensing, actuation, and the multi-input multi-output system can be found in [5,17].

By adding an harmonic disturbance signal $\mathbf{f}_{\mathrm{in}}(t)$ to the input forces (Fig. 23), the behavior of the structure can be obtained independently of the controller. After taking the discrete Fourier transforms of the signals ($\mathbf{f}_{\mathrm{in}}$, $\mathbf{f}_{\mathrm{act}}$, and $\mathbf{u}_{\mathrm{sens}}$) into the frequency domain, the sensitivity function $\mathbf{S}(\omega)$ and the process sensitivity function $\mathbf{R}(\omega)$ can be calculated [3] as

$$S_{ij}(\omega) = \frac{f_{\mathrm{act},i}(\omega)}{f_{\mathrm{in},j}(\omega)}, \qquad R_{ij}(\omega) = \frac{u_{\mathrm{sens},i}(\omega)}{f_{\mathrm{in},j}(\omega)}, \tag{15}$$

which are multi-input multi-output (*i.e.* matrix) transfer functions. Using the analytical relations of these two transfer functions

$$\mathbf{S}(\omega) = (\mathbf{I} + \mathbf{P}(\omega)\mathbf{C}(\omega))^{-1}, \tag{16}$$

$$\mathbf{R}(\omega) = \mathbf{P}(\omega)(\mathbf{I} + \mathbf{P}(\omega)\mathbf{C}(\omega))^{-1},$$

the transfer function of the original plant can be extracted as

$$\mathbf{P}(\omega) = \mathbf{R}(\omega)\mathbf{S}(\omega)^{-1}. \tag{17}$$

Here, the multi-input multi-output transfer functions of plant and controller are denoted $\mathbf{P}(\omega)$ and $\mathbf{C}(\omega)$, respectfully.

From the frequency response functions of the two out-of-plane rotations (tip and tilt), shown in Fig. 24, the resonance peaks can clearly be identified, which occur at the eigenfrequencies of the chuck. This leads to the experimentally determined eigenfrequencies, which are summarized in Table 3. It is seen that the predicted and measured frequencies are in close agreement, with a discrepancy of around 1%.
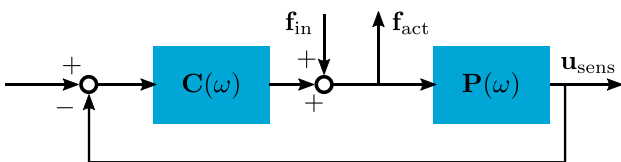

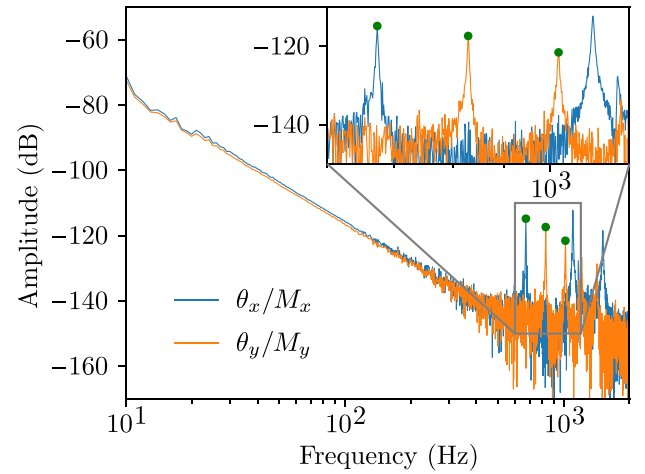**Fig. 23.** Feedback loop with indicated measurement signals for experimental validation of the stage.

Fig. 24. Frequency response functions of the two out-of-plane rotations.

Table 3
Experimental validation of the optimized design, values are in Hz.

	Numerical	Experimental	
Mode 1	667	673	−0.9%
Mode 2	837	829	+1.0%
Mode 3	1011	1021	−1.0%

4. Discussion

In the current work, topology optimization is combined with AM for a high-performance dynamic application of industry-relevant complexity. The fact that an optimal design is reached in 25 h, is paramount for practical use. When dimensions or component positions change, re-runs are necessary. The fast design time also facilitates comparative studies of different product requirements by running multiple optimizations. Especially for repeated optimization of customized products, where the design goal (*e.g.* performance) is similar, these techniques can have a huge benefit in terms of automation. In fields where time-to-market is important, a fully automated pipeline from concept to production could be made, only requiring the optimization structure to be set up once.

The superior performance of the optimized chuck as compared to reference designs (Table 2) clearly demonstrates the added benefit of combining topology optimization with AM. Recently, advances in topology optimization of 5-axis milling have been made [26,36]. It would be worthwhile to investigate the performance benefit of combining AM and topology optimization, as compared to combining milling and topology optimization, or even the combination of all three methods.

In the current design, the only manual post-processing operation required is the removal of enclosed voids. In the large central void,

two access holes were added to release the metal powder (as seen in Fig. 20), and four other small voids were removed by converting them to solid material. However, these modifications can have a detrimental effect on the final performance. In this case the effects are negligible, but this is not a certainty in general. Therefore, the avoidance of enclosed voids should be taken into account during the optimization. This is still an ongoing research topic, where promising methods have been proposed in recent years (*e.g.* [37,38]).

The optimized design is experimentally validated with a discrepancy of around 1%. This indicates that the modeling using a structured mesh that does not exactly represent the geometry still yields accurate results. However, the accuracy will most likely deteriorate for coarser mesh sizes, because the geometric error in the voxelization process will increase. Next to this, it can also be hard to model small gaps between components, which are linked to the element size, in this case 1 mm. Possible solutions include the use of substructuring for passive components [39,40].

For the application of a high-precision motion stage, the eigenfrequencies are not the only important aspect in the final performance. Accurate positioning is achieved by closed-loop feedback control, making the controller and controller–structure interaction equally important. By simultaneous optimization of both the controller and structure, even better performance in terms of bandwidth and positioning accuracy can be expected [5], which is an area for future research.

5. Conclusion

In this work, we have presented a fast and systematic process for the design of structures with high dynamic performance, exploiting the combination of additive manufacturing and topology optimization. The methodology is demonstrated using the design case of a high-precision motion system and is applicable to a wide range of industrial applications requiring high eigenfrequencies. All steps of the manufacturing process (additive manufacturing, milling, and assembly) are incorporated into the optimization procedure. This results in optimized designs that are almost directly producible. Only minimal manual modifications were required to remove enclosed voids, otherwise trapping the metal powder used in the laser powder-bed fusion process.

Specifically in the overhang filter, an improved sampling scheme was proposed to allow more freedom in the choice of overhang angle and print direction. This scheme represents the geometric overhang more accurately in a Cartesian grid and is less dependent on the orientation of the grid.

Small geometric features require a fine design resolution, which comes at a computational cost. In the current work, external components are added by voxelization into the same mesh. This has the benefit of only having one mesh, but the disadvantage is that components may only be separated from each other by a minimum gap size of one element. More effective inclusion of components for dynamic structures remains a direction for future research.

A novel cost-effective robust formulation was proposed to allow feature size control without computation of additional eigenvalue problems. By combining the eroded design field for the stiffness matrix and the dilated for the mass matrix, a worst-case estimate is obtained, effectively reducing the computational cost by a factor 3 for the calculation of eigenfrequencies. In this design case, a new optimal design is generated in 25 h using 192 CPU cores, which enables practical use and opens new opportunities for design methodology of industrial applications.

As is expected, the optimized design achieves superior performance. In the current design case of a high-precision motion stage, a performance increase of around 15% is reached as compared to conventional designs. Additionally, the optimized design is experimentally validated with a measured performance within 1% of the simulated performance. Not only does this reinforce the confidence that the performance can be predicted correctly, especially in this example with multiple components, but that also the manufacturing considerations of the optimization are sufficient for production. Using the outlined approach, this study demonstrates that the benefits of topology optimization in combination with additive manufacturing can be transferred to industrial high dynamic applications, where superior performance often is the driving factor.

Even further improvements in performance may be achieved by optimization on a system level. In the case of a high-precision motion system, the controller and the closed-loop interaction with the structure are as important as the structure itself. Therefore, this provides a valuable research direction for the next generation of dynamic systems.

CRediT authorship contribution statement

Arnoud Delissen: Writing – original draft, Visualization, Software, Methodology, Investigation, Conceptualization. **Elwin Boots:** Writing – review & editing, Investigation. **Dick Laro:** Writing – review & editing, Resources. **Harry Kleijnen:** Writing – review & editing, Writing – original draft, Resources. **Fred van Keulen:** Writing – review & editing, Funding acquisition, Conceptualization. **Matthijs Langelaar:** Writing – review & editing, Supervision, Project administration, Funding acquisition, Conceptualization.

Declaration of competing interest

One or more of the authors of this paper have disclosed potential or pertinent conflicts of interest, which may include receipt of payment, either direct or indirect, institutional support, or association with an entity in the biomedical field which may be perceived to have potential conflict of interest with this work. For full disclosure statements refer to https://doi.org/10.1016/j.addma.2022.103012.E Boots reports a relationship with MI-Partners that includes: employment. D Laro reports a relationship with MI-Partners that includes: employment. H Kleijnen reports a relationship with Additive Industries that includes: employment.

Acknowledgments

Appendix A. Proof of the robust formulation

The design sensitivities of eigenfrequency ω_i (Eq. (14)) with respect to the Young's modulus E_j and mass density ρ_j are (from, *e.g.*, [41])

$$\frac{\partial \omega_i}{\partial E_j} = \frac{1}{2\omega_i} \boldsymbol{\varphi}_i^{\mathrm{T}} \frac{\partial \mathbf{K}}{\partial E_j} \boldsymbol{\varphi}_i,$$

$$\frac{\partial \omega_i}{\partial \rho_j} = -\frac{\omega_i}{2} \boldsymbol{\varphi}_i^{\mathrm{T}} \frac{\partial \mathbf{M}}{\partial \rho_j} \boldsymbol{\varphi}_i. \tag{A.1}$$

The sensitivities of the stiffness and mass matrix (Eq. 13) relate to the unit element matrices $\mathbf{K}_0$ and $\mathbf{M}_0$ through the assembly operation, which are positive semi-definite and positive definite, respectively. This implies that the sensitivities of the assembled system matrices $\frac{\partial \mathbf{K}}{\partial E_j}$ and $\frac{\partial \mathbf{M}}{\partial \rho_j}$ are positive semi-definite.

$$\boldsymbol{\varphi}_i^{\mathrm{T}} \frac{\partial \mathbf{K}}{\partial E_j} \boldsymbol{\varphi}_i \geq 0 \quad \forall \quad \boldsymbol{\varphi}_i \neq \mathbf{0},$$

$$\boldsymbol{\varphi}_i^{\mathrm{T}} \frac{\partial \mathbf{M}}{\partial \rho_j} \boldsymbol{\varphi}_i \geq 0 \quad \forall \quad \boldsymbol{\varphi}_i \neq \mathbf{0}. \tag{A.2}$$

Generally, these quadratic forms are positive, as they are only equal to zero in specific cases of element deformation, such as no deformation or

a rigid body deformation of element j. Additionally, the eigenfrequency ω_i is positive, which means the following relations hold

$$\frac{\partial \omega_i}{\partial E_j} \geq 0 \quad \text{and} \quad \frac{\partial \omega_i}{\partial \rho_j} \leq 0. \tag{A.3}$$

From these it is evident that increasing the Young's modulus will generally result in higher eigenfrequencies and increasing the mass generally results in lower eigenfrequencies.

Appendix B. Supplementary data

Supplementary material related to this article can be found online at https://doi.org/10.1016/j.addma.2022.103012.

References

[1] S. Yoder, S. Morgan, C. Kinzy, E. Barnes, M. Kirka, V. Paquit, P. Nandwana, A. Plotkowski, R.R. Dehoff, S.S. Babu, Characterization of topology optimized Ti-6Al-4V components using electron beam powder bed fusion, Addit. Manuf. 19 (2018) 184–196, http://dx.doi.org/10.1016/j.addma.2017.12.001.

[2] M.E. Lynch, M. Mordasky, L. Cheng, A. To, Design, testing, and mechanical behavior of additively manufactured casing with optimized lattice structure, Addit. Manuf. 22 (2018) 462–471, http://dx.doi.org/10.1016/j.addma.2018.05.021.

[3] R.M. Schmidt, G. Schitter, J. van Eijk, The Design of High Performance Mechatronics, Delft University Press, Delft, 2011.

[4] T. Oomen, Advanced motion control for precision mechatronics: Control, identification, and learning of complex systems, IEEJ J. Ind. Appl. 7 (2) (2018) 127–140, http://dx.doi.org/10.1541/ieejjia.7.127.

[5] G. van der Veen, M. Langelaar, S. van der Meulen, D. Laro, W. Aangenent, F. van Keulen, Integrating topology optimization in precision motion system design for optimal closed-loop control performance, Mechatronics 47 (2017) 1–13, http://dx.doi.org/10.1016/j.mechatronics.2017.06.003.

[6] M.P. Bendsøe, O. Sigmund, Topology Optimization: Theory, Methods and Applications, first ed., Springer-Verlag, Berlin, Heidelberg, 2003.

[7] A.T. Gaynor, J.K. Guest, Topology optimization for additive manufacturing: Considering maximum overhang constraint, in: 15th AIAA/ISSMO Multidisciplinary Analysis and Optimization Conference, Atlanta, USA, 2014, pp. 1–8, http://dx.doi.org/10.2514/6.2014-2036.

[8] M. Langelaar, Topology optimization of 3D self-supporting structures for additive manufacturing, Addit. Manuf. 12 (2016) 60–70, http://dx.doi.org/10.1016/j.addma.2016.06.010.

[9] M. Hoffarth, N. Gerzen, C.B.W. Pedersen, ALM Overhang constraint in topology optimization for industrial applications, in: Proceedings of the 12th World Congress on Structural and Multidisciplinary Optimisation, Braunschweig, Germany, 2017, pp. 1–11.

[10] X. Qian, Undercut and overhang angle control in topology optimization: A density gradient based integral approach, Internat. J. Numer. Methods Engrg. 111 (3) (2017) 247–272, http://dx.doi.org/10.1002/nme.5461.

[11] J. Liu, A.T. Gaynor, S. Chen, Z. Kang, K. Suresh, A. Takezawa, L. Li, J. Kato, J. Tang, C.C.L. Wang, L. Cheng, X. Liang, A.C. To, Current and future trends in topology optimization for additive manufacturing, Struct. Multidiscip. Optim. 57 (2018) 2457–2483, http://dx.doi.org/10.1007/s00158-018-1994-3.

[12] E. van de Ven, R. Maas, C. Ayas, M. Langelaar, F. van Keulen, Overhang control based on front propagation in 3D topology optimization for additive manufacturing, Comput. Methods Appl. Mech. Engrg. 369 (2020) 1–21, http://dx.doi.org/10.1016/j.cma.2020.113169.

[13] Z.D. Ma, N. Kikuchi, H.C. Cheng, Topological design for vibrating structures, Comput. Methods Appl. Mech. Engrg. 121 (1–4) (1995) 259–280, http://dx.doi.org/10.1016/0045-7825(94)00714-X.

[14] N.L. Pedersen, Maximization of eigenvalues using topology optimization, Struct. Multidiscip. Optim. 20 (2000) 2–11, http://dx.doi.org/10.1007/s001580050130.

[15] S. Zargham, T.A. Ward, R. Ramli, I.A. Badruddin, Topology optimization: A review for structural designs under vibration problems, Struct. Multidiscip. Optim. 53 (2016) 1157–1177, http://dx.doi.org/10.1007/s00158-015-1370-5.

[16] F. Wang, B.S. Lazarov, O. Sigmund, On projection methods, convergence and robust formulations in topology optimization, Struct. Multidiscip. Optim. 43 (2011) 767–784, http://dx.doi.org/10.1007/s00158-010-0602-y.

[17] D. Laro, E. Boots, J. van Eijk, L. Sanders, Design and control of a through wall 450 mm vacuum compatible wafer stage, in: Proceedings of the 13th EUSPEN International Conference, Berlin, Germany, 2013, pp. 334–337.

[18] Additive Industries, MetalFAB1 industrial 3D printer, 2021, https://www.additiveindustries.com/systems/metalfab1. (Accessed 28 October 2021).

[19] T.E. Bruns, D.A. Tortorelli, Topology optimization of non-linear elastic structures and compliant mechanisms, Comput. Methods Appl. Mech. Engrg. 190 (26–27) (2001) 3443–3459, http://dx.doi.org/10.1016/S0045-7825(00)00278-4.

[20] K. Svanberg, The method of moving asymptotes - A new method for structural optimization, Internat. J. Numer. Methods Engrg. 24 (2) (1987) 359–373, http://dx.doi.org/10.1002/nme.1620240207.

[21] O. Sigmund, Manufacturing tolerant topology optimization, Acta Mech. Sinica 25 (2009) 227–239, http://dx.doi.org/10.1007/s10409-009-0240-z.

[22] J. Pellens, G. Lombaert, B. Lazarov, M. Schevenels, Combined length scale and overhang angle control in minimum compliance topology optimization for additive manufacturing, Struct. Multidiscip. Optim. 59 (2019) 2005–2022, http://dx.doi.org/10.1007/s00158-018-2168-z.

[23] M. Langelaar, Combined optimization of part topology, support structure layout and build orientation for additive manufacturing, Struct. Multidiscip. Optim. 57 (2018) 1985–2004, http://dx.doi.org/10.1007/s00158-017-1877-z.

[24] M. Langelaar, Integrated component-support topology optimization for additive manufacturing with post-machining, Rapid Prototyp. J. 25 (2) (2018) 255–265, http://dx.doi.org/10.1108/RPJ-12-2017-0246.

[25] E. van de Ven, C. Ayas, M. Langelaar, R. Maas, F. van Keulen, Accessibility of support structures in topology optimization for additive manufacturing, Internat. J. Numer. Methods Engrg. (2020) nme.6611, http://dx.doi.org/10.1002/nme.6611.

[26] M. Langelaar, Topology optimization for multi-axis machining, Comput. Methods Appl. Mech. Engrg. 351 (2019) 226–252, http://dx.doi.org/10.1016/j.cma.2019.03.037.

[27] J. Zhu, W. Zhang, P. Beckers, Integrated layout design of multi-component system, Internat. J. Numer. Methods Engrg. 78 (6) (2009) 631–651, http://dx.doi.org/10.1002/nme.2499.

[28] R. Budynas, K. Nisbett, Shigley's Mechanical Engineering Design, eighth ed., McGraw-Hill, 2006.

[29] J.D. Foley, A. van Dam, S.K. Feiner, J.F. Hughes, R.L. Phillips, Introduction to Computer Graphics, Addison-Wesley Professional, 1993.

[30] S. Balay, S. Abhyankar, M.F. Adams, J. Brown, P. Brune, K. Buschelman, L. Dalcin, A. Dener, V. Eijkhout, W.D. Gropp, D. Karpeyev, D. Kaushik, M.G. Knepley, D.A. May, L.C. McInnes, R.T. Mills, T. Munson, K. Rupp, P. Sanan, B.F. Smith, S. Zampini, H. Zhang, H. Zhang, PETSc Web page, URL https://www.mcs.anl.gov/petsc.

[31] V. Hernandez, J.E. Roman, V. Vidal, SLEPC: A scalable and flexible toolkit for the solution of eigenvalue problems, ACM Trans. Math. Softw. 31 (3) (2005) 351–362, http://dx.doi.org/10.1145/1089014.1089019.

[32] M. Geradin, D.J. Rixen, Mechanical Vibrations: Theory and Application to Structural Dynamics, third ed., John Wiley & Sons, Ltd, 2015.

[33] D. Trillet, P. Duysinx, E. Fernández, Analytical relationships for imposing minimum length scale in the robust topology optimization formulation, Struct. Multidiscip. Optim. 64 (2021) 2429–2448, http://dx.doi.org/10.1007/s00158-021-02998-w.

[34] J. Ahrens, B. Geveci, C. Law, ParaView : An end-user tool for large-data visualization, in: Visualization Handbook, Elsevier, 2005, pp. 717–731.

[35] G. Misiun, E. van de Ven, M. Langelaar, H. Geijselaers, F. van Keulen, T. van den Boogaard, C. Ayas, Topology optimization for additive manufacturing with distortion constraints, Comput. Methods Appl. Mech. Engrg. 386 (2021) 114095, http://dx.doi.org/10.1016/j.cma.2021.114095.

[36] J.K. Guest, M. Zhu, Casting and milling restrictions in topology optimization via projection-based algorithms, in: Proceedings of the ASME 2012 IDETC/CIE, Chicago, USA, 2012, pp. 913–920, http://dx.doi.org/10.1115/DETC2012-71507.

[37] Q. Li, W. Chen, S. Liu, L. Tong, Structural topology optimization considering connectivity constraint, Struct. Multidiscip. Optim. 54 (2016) 971–984, http://dx.doi.org/10.1007/s00158-016-1459-5.

[38] A.T. Gaynor, T.E. Johnson, Eliminating occluded voids in additive manufacturing design via a projection-based topology optimization scheme, Addit. Manuf. 33 (2020) 1–13, http://dx.doi.org/10.1016/j.addma.2020.101149.

[39] D. de Klerk, D.J. Rixen, S.N. Voormeeren, General framework for dynamic substructuring: History, review and classification of techniques, AIAA J. 46 (5) (2008) 1169–1181, http://dx.doi.org/10.2514/1.33274.

[40] H.S. Koh, J.H. Kim, G.H. Yoon, Efficient topology optimization of multicomponent structure using substructuring-based model order reduction method, Comput. Struct. 228 (2020) 1–16, http://dx.doi.org/10.1016/j.compstruc.2019.106146.

[41] R.T. Haftka, Z. Gürdal, M.P. Kamat, Elements of Structural Optimization, Vol. 11, Springer Science+Business Media Dordrecht, 1990, http://dx.doi.org/10.1007/978-94-011-2550-5.